

Photophysics of O₂ excited by tunable laser radiation around 193 nm

B. L. G. Bakker^{a)} and D. H. Parker

Department of Molecular and Laser Physics, University of Nijmegen, Toernooiveld 1, 6525 ED Nijmegen, The Netherlands

(Received 21 October 1999; accepted 10 December 1999)

The photodissociation/ionization dynamics of O₂ around 193 nm have been studied using a narrowband tunable ArF excimer laser and the velocity map imaging technique. Angular and kinetic energy distributions of the product O⁺ ions and O(³P₂) atoms are recorded and analyzed. The production of O(³P₂) atoms is resonance enhanced on the one-photon level by the B³Σ_u⁻(*v*=4) state, which is part of the B³Σ_u⁻←X³Σ_g⁻ Schumann–Runge bands. Angular distribution measurements for individual rotational levels of the B state yield values for the anisotropy parameter, β_{SR}, which are in good agreement with the values predicted by independent measurements of predissociation lifetimes from spectral linewidths. An average value of β=0.48 is found for the underlying Herzberg continuum at 193 nm. O₂⁺ production is enhanced on the two-photon level via members of the *nsσ_g(n-1)dπ_g¹Σ_g⁺* Rydberg series terminating at higher vibrational levels of the ion. The high Rydberg states autoionize into the O₂⁺ X²Π_g ground state or absorb one more photon and then autoionize into the A²Π_u and b⁴Σ_u⁻ states of O₂⁺, which subsequently fluoresce. Production of O⁺ from one- and two-photon dissociation of the O₂⁺ formed after two-photon absorption is also observed and characterized. © 2000 American Institute of Physics. [S0021-9606(00)01709-8]

I. INTRODUCTION

Molecular oxygen plays a central role in many research fields including atmospheric physics, combustion analysis, and in fundamental studies of the quantum mechanics of small molecules. In this article we describe the photophysics of molecular oxygen excited by tunable radiation around 193 nm, a wavelength falling within the Schumann–Runge bands,¹ the dominant photoabsorption system in the Earth's atmosphere. Molecular oxygen dissociates on absorbing this vacuum ultraviolet radiation. The speed and angular distribution of the atomic products are determined here by the velocity map imaging technique.² Predissociation lifetimes of the B³Σ_u⁻ excited electronic state and those of the underlying Herzberg continuum³ can be determined from the angular distribution anisotropy. These values are compared with previously measured rates from spectroscopic linewidths.⁴

A narrowband tunable ArF laser generates the radiation used in this study. When this type of laser is focused it is easily capable of driving not only one-photon absorption but also higher order multiphoton absorption and ionization processes. Neutral and ionic products are formed, their analysis yields information on the high-energy states of O₂ and O₂⁺. A rich array of interesting and unexpected photodissociation / ionization steps are found to take place following multiphoton excitation, many of which provide new insight into the basic photophysics of molecular oxygen. Furthermore, these newly identified mechanisms can be of practical importance because tunable ArF lasers are very often employed in diagnostics of combustion processes⁵ under conditions where the same multiphoton events can take place.

Competition between dissociation and ionization during multiphoton absorption is a topic of basic interest in itself in laser ionization studies. Most relevant to this work, Hill and co-workers⁶ have studied the competition between the ionization and fragmentation channels in O₂ following excitation by a focused, broadband ArF laser using relatively low-resolution time-of-flight detection of O⁺. Our higher resolution velocity mapping technique, supplemented by detection of nascent O(³P₂) atoms, leads us to a different interpretation of molecular oxygen photophysics in this wavelength region. These interpretations become much more straightforward when using tunable narrowband instead of broadband radiation.

Velocity map imaging has proven to be a powerful method for investigation of photodynamical processes in molecules.² The technique is ideally suited for simple diatomic molecules such as O₂ because the large vibrational spacing and limited number of possible atomic product states results in a unique kinetic energy release (KER) for each final quantum state channel. Besides providing the product quantum state distributions from the kinetic energy distribution, the angular distributions of the fragments are also measured, allowing in many cases an enhanced discrimination between the different decay channels. For a rapid one-photon dissociation the product angular distributions *I*(θ) is given by⁷

$$I(\theta) \propto 1 + \beta P_2(\cos \theta), \quad (1)$$

where θ is the angle between the laser polarization and the velocity vector of the particles and P₂ is the second-order Legendre polynomial. The anisotropy parameter β ranges from limiting values -1 to 2, corresponding to a perpendicular (Π←Σ) and parallel (Σ←Σ) transition, respectively. If

^{a)}Electronic mail: bernard@sci.kun.nl

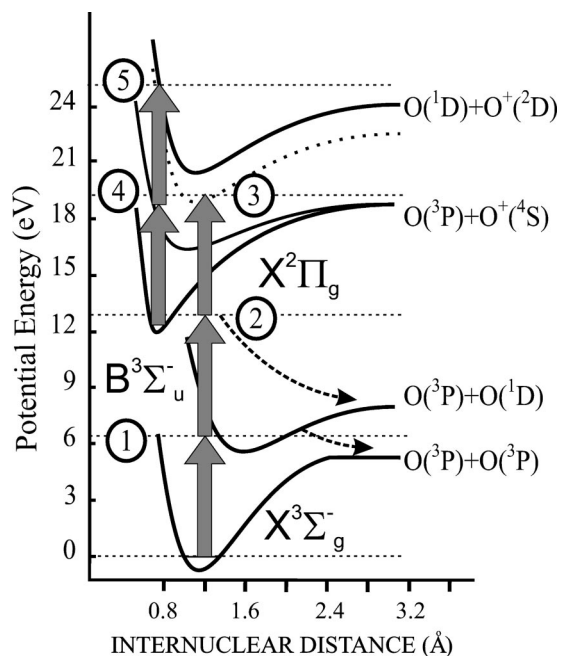


FIG. 1. Schematic potential energy curves for O_2 and O_2^+ .

the lifetime τ of the excited state is similar to the parent molecule rotational period T and the associating rotational frequency $\nu=1/T$ of that state, the anisotropy parameter is given by⁸

$$\beta_{||} = 2 \frac{(\nu^2 \tau^2 + 1)}{(4\nu^2 \tau^2 + 1)} \quad (2)$$

for a parallel transition and

$$\beta_{\perp} = -1 \frac{(\nu^2 \tau^2 + 1)}{(4\nu^2 \tau^2 + 1)} \quad (3)$$

for a perpendicular transition. The slow dissociation limiting values for these anisotropy parameters are $\beta_{||}=0.5$ and $\beta_{\perp}=-0.25$. Measurement of β for each channel thus provides information on the symmetry of the electronic states involved in the absorption process and their lifetimes with respect to rotation.

Shown schematically in Fig. 1 are the O_2 potential energy curves most relevant to this study. The bond energy of the ground electronic state, $X^3\Sigma_g^-$, is 5.115 eV and corresponds to the asymptotic limit of two $O(^3P)$ atoms. In the ultraviolet region of the O_2 spectrum extremely weak and sharp absorption from the $X^3\Sigma_g^-$ ground electronic state to the three electronically excited Herzberg states ($A^3\Sigma_u^+$, $A'^3\Delta_u$, and $c^1\Sigma_u^-$) take place which change over at 242 nm to the Herzberg continuum (242–180 nm).³ Although optically forbidden, photoabsorption / dissociation of O_2 due to the Herzberg continuum is the primary source of $O(^3P)$ atoms in the stratosphere.⁹ Deeper into the UV region the strong but predissociated bands of the Schumann–Runge system (205–130 nm) arise from the optically allowed $B^3\Sigma_u^- \leftarrow X^3\Sigma_g^-$ transition. They change over to a continuum below 175 nm corresponding to the second dissociation limit, $O(^3P)+O(^1D)$ at 7.08 eV. Predissociation of bound

levels of the $B^3\Sigma_u^-$ state, primarily by the $^5\Pi$ state, takes place resulting in the production of two $O(^3P)$ atoms.

At higher energies in the O_2 spectrum a series of optically allowed mixed valence-Rydberg *ungerade* states converging on the $O_2^+ X^2\Pi_u$ ground state (ionization potential = 12.08 eV) are observed.¹⁰ Several *gerade* Rydberg series¹¹ converging on the ground state of O_2^+ have been characterized using two-photon resonance enhanced multiphoton ionization, (2+1) REMPI. Mixing of those molecular Rydberg states with repulsive valence states can lead to rapid predissociation. The possible dissociation limits $O(^3P)+O(^3P)$, $O(^1D)+O(^3P)$, $O(^1D)+O(^1D)$, and $O(^1S)+O(^3P)$ fragments all lie within the energy sum of two ArF laser photons. Because this energy sum also exceeds the ionization potential of O_2 , two-photon absorption can lead via direct ionization to the formation of ground state $X^2\Pi_u O_2^+(v^+=0,1,2,3)$. The ion has a dissociation energy of 6.66 eV, slightly higher than the 6.4 eV photon energy, thus all vibrational levels of $O_2^+ X^2\Pi_u$ higher than $v^+=0$ can be photodissociated, leading to $O(^4S)+O(^3P)$ products (18.733 eV limit). Absorption of two ArF laser photons by O_2^+ can also take place as shown in this study, exciting the $X^2\Pi_u v^+=0$ level to 24.90 eV which lies above the first five (O^+ + O) dissociation limits (18.733, 20.700, 22.937, 23.057, and 24.025 eV). One possibility, dissociation to the $O^+(^2D)+O(^1D)$ limit at 24.025 eV, is shown in Fig. 1. In summary, O^+ production mechanisms shown in Fig. 1 include one- and two-photon dissociation of O_2^+ , while $O(^3P)$ atoms can be formed after the absorption of one or more photons. Numerous other mechanisms could lead to O^+ formation including ion-pair formation, or nonresonant three-photon ionization of O atoms as suggested by Yang, Hill, and Dixit.⁶ These are not observed, however, as shown in this study.

II. EXPERIMENT

A detailed description of the velocity mapping apparatus has been reported elsewhere² thus only a brief summary of the experimental details will be given here. A pulsed and skimmed supersonic beam of pure O_2 is directed down the axis of a time-of-flight (TOF) mass spectrometer and crossed at right angles by the line-narrowed ($\Delta\nu \sim 0.5 \text{ cm}^{-1}$) ArF excimer laser. The 193 nm light (15 ns pulse width, 25 mJ per pulse, $\sim 5 \times 10^{16}$ photons) was focused with a 35 cm lens on to the molecular beam resulting in an intensity of $\sim 5 \times 10^{10} \text{ W/cm}^2$. The line-narrowed scanning range is 51 600–51 800 cm^{-1} and under the best conditions, a broadband component with integrated intensity at least equal to that of the line-narrowed accompanies the narrowband output. The laser can also be operated fully broadband ($\Delta\nu \sim 200 \text{ cm}^{-1}$) by blocking the oscillator grating.

A series of dichroic mirrors used to direct the beam serve also to attenuate the horizontal component of the initially unpolarized beam and result in >95% vertical polarization at the interaction zone. The atomic products of predissociation were monitored by two-photon resonance enhanced multiphoton ionization [(2+1) REMPI] of $O(^3P_2)$ using the 226 nm output of a counterpropagating second Nd:YAG pumped frequency-doubled dye laser operating with Coumarin 47. The probe laser beam was focused on to

the molecular beam using a 20 cm focal length lens and had a typical energy of less than 1 mJ per pulse. The detection laser pulse arrived ~ 20 ns after the photolysis pulse. To ensure equal detectivity for all velocity groups the detection laser wavelength was scanned repetitively across the Doppler profile of the (2+1) REMPI transition. The formed ions were extracted from the ionization region through a grounded time-of-flight tube and crushed onto a two-dimensional microchannel plate / phosphor screen detector read by a charge-coupled device (CCD) camera. Mass selectivity was achieved by pulsing on the gain of the detector as the O⁺ ions arrive. Typically, 25 000 laser shots were used to produce the final raw image which was then inverted using an inverse two-dimensional (2D)–three-dimensional (3D) Abel transformation.

The overall quality of the images obtained using the excimer laser, particularly those taken in combination with the additional O(³P₂) detection laser, were not as high as images obtained using Nd-YAG pumped dye lasers. This could partially arise from insufficient time-focusing (“pancaking” of the 3D image before it hits the detector) due to the longer pulse length of the excimer (15 ns in comparison to ~ 3 ns from doubled-dye lasers pumped by a Nd:YAG laser). More likely, the problem arises from the rectangular beam geometry (3 by 1 cm) of the excimer laser. The laser is focused with a simple plano-convex lens on to the molecular beam, with the longer laser beam axis lying parallel to the time-of-flight axis. Because the laser beam spatial pattern shows shot-to-shot fluctuations, the position of the ion origin will be spread along the TOF axis. Velocity mapping magnifies the image by slightly different factors dependent on this position, which will thus lower the sharpness of the image. Shot-to-shot fluctuations in the focal position are particularly disturbing for the two-laser experiments for obvious reasons. Overall, the energy resolution of the excimer-laser-produced images is estimated to be ~ 60 meV at 1 eV kinetic energy release, compared to ~ 30 meV for images produced by a Nd:YAG pumped dye laser.¹²

III. RESULTS

Typical images obtained with the 193 nm light alone and along with the O(³P₂) detection laser are shown in Fig. 2. Raw half-images are presented on the left-hand sides of Fig. 2(a) for the one-laser result and Fig. 2(c) for the two-laser result, while the Abel-inverted half-image is shown on the right side of Figs. 2(b) and 2(d). The images show a series of sharp concentric rings whose velocity are directly calibrated using the known³ O(³P₂) atom signals from the detection laser alone, which also produces O(³P₂) atoms from the photodissociation of O₂ via one- and two-photon absorption. The radius of the ring is proportional to the velocity of the products, so after calibration the kinetic energy release corresponding to all other rings is determined. Accuracy is high enough that the number of photons absorbed can be distinguished in the photodissociation processes. Distributions of the total kinetic energy release (i.e., twice the atom kinetic energy) extracted from the raw images Figs. 2(a) and 2(b)

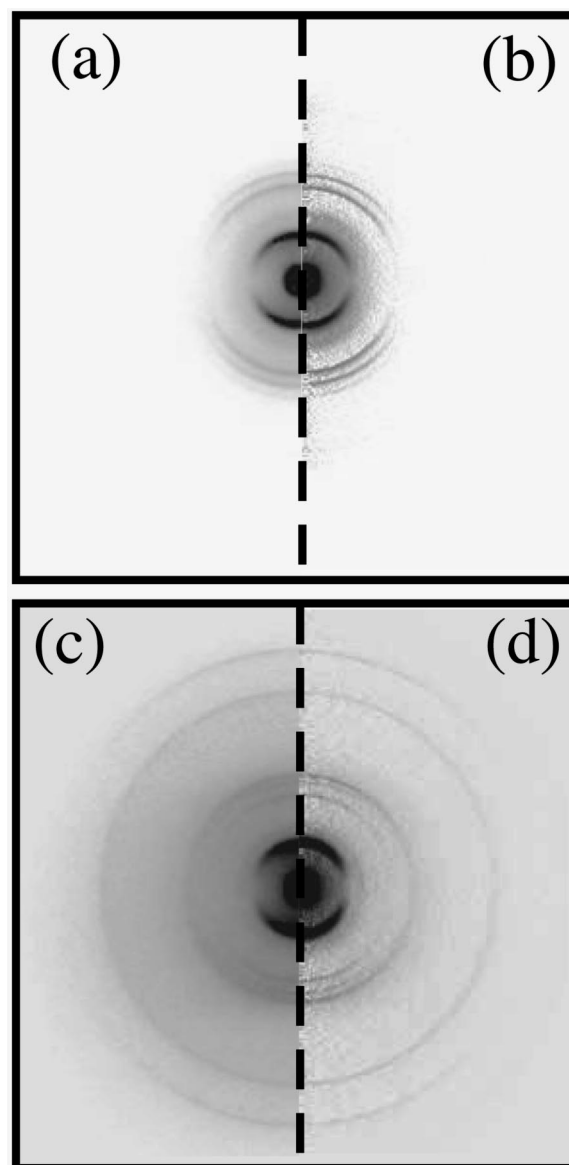


FIG. 2. Raw (left side) and Abel-inverted (right side) O⁺ images: (a) and (b) for 193 nm laser excitation of O₂; (c) and (d) for 193 nm excitation of O₂ with O(³P₂) detection.

are shown in Figs. 3(a) and 3(b), respectively. These are obtained from the inverted image by integrating over the full angular distribution.

As seen in Fig. 2, each dissociation channel produces some signal along the vertical axis. The spectral behavior of the kinetic energy distribution can be investigated by fixing the detection laser on top of the O(³P₂) 2+1 REMPI wavelength, so that atoms flying along the direction of the laser polarization (no Doppler shift) are detected. The image processing software is then set to average a vertical slice of the image approximately 10 pixels wide. The computer software compresses and stores this slice as an array 1 pixel wide (averaging the approximate 10 pixels) by 286 pixels high. For each following array the dissociation laser wavelength is stepped. The top and bottom halves (upward and downward traveling ions) of the 2D array of velocity distribution versus dissociation laser frequency are then averaged. The top half

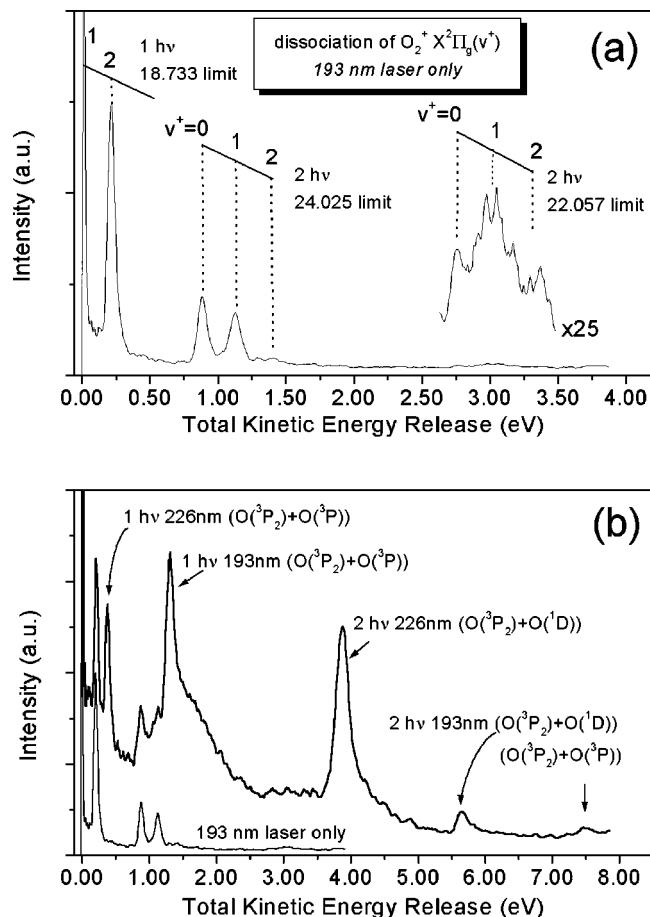


FIG. 3. Kinetic energy distributions for the images shown in Fig. 2.

of such an array for O^+ [and $O(^3P_2)$] detection from O_2 is shown in Fig. 4.

The analysis of the different dissociation channels as a function of laser bandwidth and frequency will be discussed for each channel separately. First, the general features of the images will be summarized. With the 193 nm laser working in the broadband mode features are seen in the 0–0.40 and 0.80–1.50 eV range along with very weak features in the 2.70–3.50 eV range, as seen in Fig. 3(a). These results are in

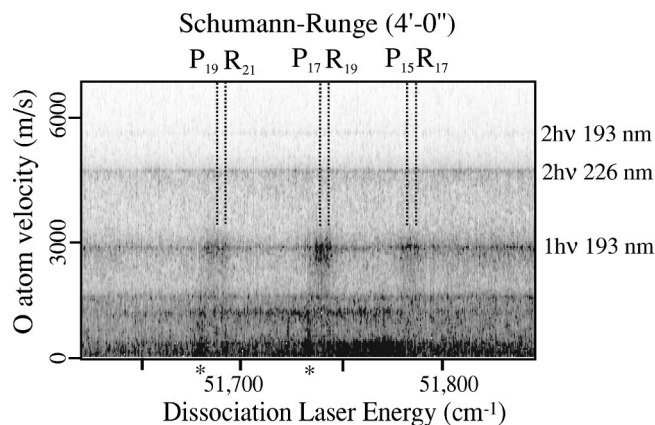


FIG. 4. Velocity distribution spectrum of O_2 . O atom velocity vs dissociation laser wavelength. Vertical lines indicate the Schumann–Runge ($4'-0''$) P and R branches, the asterisk indicates the two-photon Rydberg states.

qualitative agreement with the time-of-flight results of Yang, Hill, and Dixit⁶ using also a broadband laser, except their TOF resolution was too low to resolve the individual peaks seen in Fig. 3(a). The weaker signals around 3 eV were not reported. When the ArF laser is operated in the narrowband mode (regardless of wavelength), essentially the same image is observed, but the signals in the 0.80–1.50 and 2.70–3.50 eV range are around five times weaker.

On adding the $O(^3P_2)$ detection laser several new rings appear in the image, mainly at higher energies than the 193 nm laser-only signals. Two peaks, labeled in Fig. 3, are due to the 226 nm detection laser only and correspond to one-photon dissociation [creating $O(^3P_2)+O(^3P)$ products] and two-photon dissociation [creating $O(^3P_2)+O(^1D)$ products] of O_2 . Three other rings correspond to dissociation at 193 nm by one-photon absorption [creating $O(^3P_2)+O(^3P)$ products, 1.29 eV total KER] and by two-photon absorption [creating $O(^3P_2)+O(^1D)$, 5.65 eV; and $O(^3P_2)+O(^3P)$ products, 7.62 eV]. A broad shoulder to higher energy accompanying the 193 nm one-photon dissociation signal grows in strength relative to the main peak at 1.29 eV total KER when the laser is operated narrowband and resonant with a Schumann–Runge (SR) transition. This is probably due to space-charge effects in the focus of the 226 nm detection laser. Note that with the 193 nm laser alone (broadband or narrowband), no signal appears at 1.29 eV, indicating that nonresonant three-photon ionization of $O(^3P)$ atoms by the excimer laser does not take place to any significant extent.

IV. DISCUSSION

In the following sections the photophysical process observed is discussed according to how many photons have been absorbed by either O_2 or O_2^+ . These different stages are labeled in Fig. 1 as: (1) one-photon absorption, (2) two-photon absorption, and (3) three-photon absorption by O_2 , and (4) one-photon absorption and (5) two-photon absorption by O_2^+ .

A. One-photon absorption at 193 nm by O_2

The photodissociation and photoionization of molecular oxygen in the vacuum ultraviolet, especially predissociation and direct dissociation via the strong Schumann–Runge (SR) bands and continuum, is an important process in our atmosphere and has accordingly received much attention in the literature. Recent studies on the photodissociation of O_2 via the Schuman–Runge bands have been reported by Lin *et al.*¹³ Huang and Gordon¹⁴ and Eppink *et al.*¹⁵ for the SR continuum, and by Leahy *et al.*,¹⁶ Gibson *et al.*,¹⁷ and Matsumi and Kawasaki¹⁸ for the SR bands. Tonokura *et al.*¹⁹ and Buijsse *et al.*²⁰ have reported similar studies for the lower lying Herzberg continuum. Information on one-photon dissociation is obtained from velocity map imaging by examining the KER = 1.29 eV peak labeled in Fig. 3(b). Most relevant to this study, Lewis, Gibson, and Dooley⁴ have examined predissociation mechanisms in the SR bands and extracted the lifetime broadened linewidths from the absorption spectrum. In the 193 nm region the SR bands are weak due to poor Franck–Condon overlap (σ for excitation of $N=15-19$ to

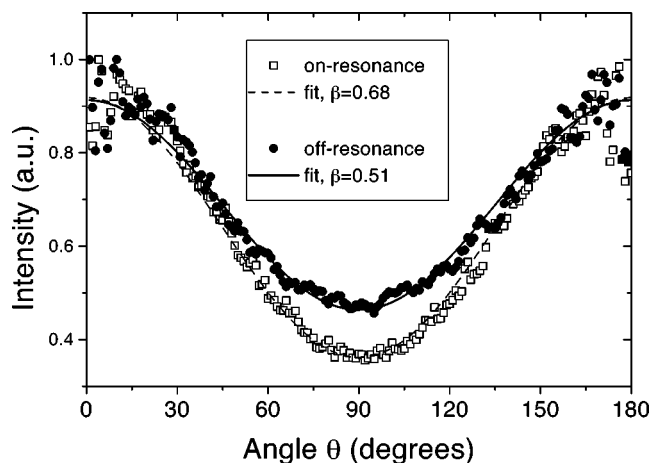


FIG. 5. Angular distributions for 193 nm one-photon dissociation of O₂.

$B(v=4) \sim 2 \times 10^{-20} \text{ cm}^{-2}$) but the underlying, optically forbidden, Herzberg continuum (HC) is a factor of ~ 3000 weaker ($\sigma \sim 7 \times 10^{-24} \text{ cm}^{-2}$) than the SR resonances. With the ArF laser tuned on resonance, the narrowband component will thus strongly favor the SR band, but the always-present broadband component of the laser radiation still makes a significant contribution. All molecules can absorb the broadband component via the HC, while only the small fraction of the resonant high N states can contribute to the SR signal.

The tunable ArF laser can excite only the higher rotational levels ($N=15, 17, 19, 21, 23$) of ground state O₂ to the $v=4$ level of the $B^3\Sigma_u^-$ state. Despite the use of a supersonic pulsed expansion, sufficient population remains in these higher J levels to observe an enhanced O(³P₂) signal on scanning through the resonances, as shown in the 2000 m/s region of Fig. 4. Independent measurements¹⁵ of the pulsed valve expansion indicate that the vast majority of rotational population in the beam after the expansion is in the $N=1, 3$, and to a much less extent the $N=5$ state. At room temperature the populations of $N=15, 17, 19$, and 21 is 8%, 6%, 4%, and 2%, respectively, and after the expansion these fractional populations are reduced significantly by an unknown amount.

Figure 5 shows the angular distributions for the one-photon dissociation signal at 1.29 eV when using broadband radiation and narrowband radiation resonant with a SR band, in this case the $P(17)$ line at $51\,736 \text{ cm}^{-1}$. Fitting to Eq. 1 yields $\beta_{\text{on}} = 0.69 \pm 0.05$ for the narrowband, on-resonance laser and $\beta_{\text{BB}} = 0.54 \pm 0.05$ for the broadband radiation. Not shown in Fig. 5 is $\beta_{\text{off}} = 0.51 \pm 0.05$ for narrowband, off-resonance laser excitation. Table I lists β_{on} values measured

for the $P(15)$, $P(17)$, and $P(19)$ transitions corresponding to the final state rotational quantum numbers $N'=14$, $N'=16$, and $N'=18$, respectively. Also presented in Table I are the corresponding calculated rotational period T and lifetime τ from spectral linewidth measurements of Lewis, Gibson, and Dooley.⁴ Filling the values of T and τ into formula (2) gives the calculated classical value of the anisotropy parameter β_{calc} . It should be noted that the $P(N'-1)$ branches are only $\sim 6 \text{ cm}^{-1}$ separated from the $R(N'+1)$ transitions, where N' is the rotational quantum number of the $B^3\Sigma_u^-$ state, while the natural linewidths of these transitions are $\sim 4 \text{ cm}^{-1}$. It is thus not possible to excite a single N' state and therefore some mixing of the state 4 quanta higher than the value listed in Table I will take place.

The measured beta values β_{on} show a different value in Table I than the expected β_{calc} . This can be explained by the fact that the ArF laser has an underlying broadband component when used in narrowband mode. Correction of the measured β_{on} values for the broadband component of the laser beam can be done very qualitatively in the following manner. The broadband (BB) β value, which results from the combination of SR and HC contributions, is $\beta_{\text{BB}} = 0.54 \pm 0.05$. A measured narrowband β value is assumed to result from $\frac{1}{2}$ narrowband excitation and $\frac{1}{2}$ broadband excitation. The corrected beta value for the HC, β_{HC} , can be determined using the corresponding expression $\beta_{\text{off}} = \frac{1}{2}\beta_{\text{HC}} + \frac{1}{2}\beta_{\text{BB}}$. The measured value $\beta_{\text{off}} = 0.51 \pm 0.05$ implies that the average value of beta for the Herzberg continuum is $\beta_{\text{HC}} = 0.48 \pm 0.10$. Off resonance, the β_{HC} value appears to be raised by the broadband component while on resonance, the experimental β_{on} value is lowered by the broadband component. Because of the large error bars these values are extremely qualitative. The same method is used to derive the beta value for the SR transitions when the laser is set on-resonance. Now the expression $\beta_{\text{on}} = \frac{1}{2}\beta_{\text{SR}} + \frac{1}{2}\beta_{\text{BB}}$ is used. As seen in Table I, good agreement is found between the corrected β_{SR} values from the angular distributions and those from the linewidth measurements β_{calc} . Leahy *et al.*¹⁶ also found good agreement between their measured beta parameter and beta predicted from the corresponding linewidth measurement, for the $B^3\Sigma_u^-$ ($v=7, N'=4$) state.

The fractional population of the $N=15, 17$, and 19 states can be estimated by combining the values for $\beta_{\text{HC}} = 0.48$, the average β value for SR ($\langle\beta_{\text{SR}}\rangle = 0.75$) and the relative absorption strengths. Linewidths of the 6 (P and R) SR bands are $\sim 4 \text{ cm}^{-1}$ full width at half-maximum each, thus the SR components can absorb $\sim 12\%$ of the laser light, but with 3000 times more absorption strength than the HC component. Assuming that $\beta_{\text{BB}} = \langle\beta_{\text{SR}}\rangle(0.12)3000(1-f)$

TABLE I. Measured (β_{on}), predicted (β_{calc}) and corrected (β_{SR}) anisotropy parameters for selected rotational levels N' of the $B^3\Sigma_u^-$ ($v=4$) states. T is the N' state rotational period and τ the state lifetime obtained from the linewidth measurements of Lewis, Gibson, and Dooley (Ref. 4).

N'	β_{on}	Linewidth(cm^{-1})	$\tau(10^{-12} \text{ s})$	$T(10^{-12} \text{ s})$	β_{calc}	β_{SR}
14	0.62 ± 0.05	3.68	1.44	1.53	0.83	0.70
16	0.68 ± 0.05	3.81	1.39	1.34	0.78	0.82
18	0.63 ± 0.05	3.79	1.40	1.20	0.73	0.72

+ $\beta_{\text{HC}}(0.88)(1)(f)$ where f is the fractional population of the $N < 15$ states yields a value of $f = 99.96$. A fractional population in the high N levels of only 0.04% is thus sufficient to account for the observed SR contributions. Alternatively, it is only because of the very strong cooling of the high N states in the supersonic expansion that an estimate of β_{HC} is possible.

Beta values for $\text{O}(^3P_2)$ atoms produced from dissociation of O_2 via the Herzberg continuum for dissociation at 226 and 204 nm of $\beta_{\text{HC}} = 0.64$ and 0.87, respectively, have been reported previously.³ The value reported here for beta at 193 nm of $\beta_{\text{HC}} = 0.48$ fits in well with theoretical analysis of the Herzberg continuum given in Ref. 3. Of the three components active in the HC, the $A\ ^3\Sigma_u^+ \leftarrow X\ ^3\Sigma_g^-$ transition is dominant, especially at shorter wavelengths because the $A'\ ^3\Delta_u \leftarrow X\ ^3\Sigma_g^-$ and $c\ ^1\Sigma_u^- \leftarrow X\ ^3\Sigma_g^-$ transitions reach their maximum at longer wavelengths than the $A\ ^3\Sigma_u^+ \leftarrow X\ ^3\Sigma_g^-$. With progressively shorter wavelengths it is expected that the dissociation will approach the sudden-recoil limit³, in which case the $j=2$ atoms should tend toward a more perpendicular angular distribution. While a prediction for β in the sudden recoil limit has not been made for 193 nm dissociation, the present value fits well in the suggested trends, and with preliminary results from an extensive theoretical analysis by Groenboom and A. van der Avoird.²¹ A more complete study including β values for the $j=1$ and $j=0$ states is desirable. Matsumi and Kawasaki¹⁸ have reported branching ratios for $j=2:1:0$ for broadband ArF laser radiation of 0.47:0.31:0.22.

B. Two-photon absorption by O_2

Two-photon excitation by the tunable ArF laser covers 103 200–103 600 cm^{-1} while the ionization energy²² lies at 97 347 cm^{-1} . In this energy range two processes can thus occur, dissociation to neutral, ground-state atoms or (auto-)ionization to form O_2^+ . Ionization producing O_2^+ in the $v^+ = 0-3$ vibrational levels occurs either by direct two-photon absorption or by two-photon excitation to autoionizing Rydberg states converging on either the ground state or excited electronic states of the ion. Photodissociation by two ArF laser photons exceeds the dissociation limits of $[\text{O}(^3P) + \text{O}(^3P), 5.115\ \text{eV}]$, $[\text{O}(^1D) + \text{O}(^3P), 7.08\ \text{eV}]$, $[\text{O}(^1D) + \text{O}(^1D), 9.05\ \text{eV}]$ and $[\text{O}(^1S) + \text{O}(^3P), 9.26\ \text{eV}]$.

Dissociation to neutral ground state atoms by two-photon absorption will first be discussed. This process is probed in this study by detection of $\text{O}(^3P_2)$ atoms, which gives information on all but the $\text{O}(^1D) + \text{O}(^1D)$ dissociation channel. Results are shown in Fig. 3 where two-photon dissociation to form $\text{O}(^3P) + \text{O}(^1D)$ (5.74 KER) and $\text{O}(^3P) + \text{O}(^3P)$ (7.71 eV KER) are indicated. This is a two-laser experiment with a separate detection laser which is always much less efficient than a one-laser experiment. Despite this, the two-photon dissociation channel to $\text{O}(^3P) + \text{O}(^1D)$ is one of the strongest signals suggesting that this is the most probable event following two-photon absorption. This corroborates the finding of van der Zande *et al.*,²³ who found that the large majority of O_2 molecules excited to an energy above $v^+ = 2$ of the ion dissociate instead of ionize. In their

experiments O atoms from charge exchange collisions of $\text{O}_2^+ a\ ^4\Pi_u$ ions with Cs were measured and evidence was found for the production and predissociation of lower vibrational levels of the $\text{H}^3\Pi_u(3s\sigma_g)$ Rydberg state which lie in the same energy region as probed in this study. In the O atom KER curves the $\text{O}(^1D) + \text{O}(^3P)$ channel was strongest but evidence was found for activity in all accessible dissociation channels. In the present work which prepares levels of overall *gerade* symmetry the $\text{O}(^1D) + \text{O}(^3P)$ channel is again strongest. No signal is seen in Fig. 3 at 3.57 eV for activity in the accessible $\text{O}(^1S) + \text{O}(^3P)$ channel.

While the formation of O_2^+ was not directly monitored in this study the O^+ images shown in Fig. 2(a) reveal information on which $\text{O}_2^+(v^+)$ states are formed. The O_2^+ dissociation data (next section) indicate that mainly $v^+ = 0, 1$, and 2 vibrational levels of ground electronic state O_2^+ are produced, although $v^+ = 3$ production is energetically allowed. Inspection of Fig. 4 for these dissociation channels show that there is no striking wavelength dependence for production of the specific $v^+ = 0, 1$, and 2 states of $\text{O}_2^+ X\ ^2\Pi_g(v^+)$. There is, however, structure in Fig. 4 in the region of zero velocity, which is due mainly to leakage of O_2^+ signal through the front channel plate in the 2D detector, whose gain has been gated to select the O^+ mass. Peaks seen at 51 678 and 51 730 cm^{-1} (marked with an asterisk in Fig. 4) are assigned to the $6s-5d\ ^3\Sigma_g^-(v=5, \Omega=1/2)$ and $9s-8d\ ^3\Sigma_g^-(v=4, \Omega=3/2)$ Rydberg levels converging to the $v^+ = 5$ and $v^+ = 4$ levels of the X state of the ion, respectively. Pratt, Dehmer, and Dehmer²⁴ characterized the lower states of this same $s-d$ complex previously. A more complete assignment of these and weaker states observed in the ArF tuning window will be discussed in a separate publication.²⁵ These levels serve as stable platforms for absorption of a third ArF laser photon, as discussed in the following.

C. Three-photon absorption by O_2

Three-photon absorption by O_2 takes place when the laser is resonant with the $ns-(n-1)d\ ^3\Sigma_g^-$ two-photon allowed Rydberg states. This leads to enhanced production of O_2^+ ions, as seen in the zero velocity region of Fig. 4. Previous studies have shown the same states are detectable by four-wave mixing²⁶ and by laser-induced fluorescence²⁷ which must arise from electronically excited O_2^+ ions. These electronically excited O_2^+ ions are reachable only by three-photon absorption by neutral O_2 . A fraction of the O_2^+ ions must be formed in the $A\ ^2\Pi_u$ excited electronic states that subsequently fluoresce in the UV. Visible fluorescence presumably due to $a\ ^4\Pi - b\ ^4\Sigma^-$ transitions has also been observed.²⁷ Laser-induced fluorescence following excitation of these states has been previously observed in ArF laser based diagnostics studies⁵ but the states are assigned here for the first time. Unfortunately, a velocity map image was not obtained with the tunable ArF laser resonant on one of the two listed bands. Images obtained for states of the same series with slightly lower energies indeed show the production of O_2^+ in higher vibrational levels of the A state²⁸ following three-photon absorption.

TABLE II. Dissociation limits of O₂⁺ and the correlating molecular states.

Dissociation products	Energy (eV)	Molecular states
O ⁺ (⁴ S)+O(³ P)	18.733	^{2,4,6} (Σ ⁺ ,Π) _{g,u}
O ⁺ (⁴ S)+O(¹ D)	20.700	⁴ (Σ ⁻ ,Π,Δ) _{g,u}
O ⁺ (² D)+O(³ P)	22.057	^{2,4} (Σ ⁻ ,Σ ⁺ ,Π,Δ,Φ) _{g,u}
O ⁺ (⁴ S)+O(¹ S)	22.923	⁴ Σ ⁻ _{g,u}
O ⁺ (² P)+O(³ P)	23.750	^{2,4} (Σ ⁻ ,Σ ⁺ ,Π,Δ) _{g,u}
O ⁺ (² D)+O(¹ D)	24.025	² (Σ ⁻ ,Σ ⁺ ,Π,Δ,Φ,Γ) _{g,u}

D. Photodissociation of O₂⁺

Molecular oxygen ions are created in the $X(v^+=0, 1, 2, 3)$ states following two-photon, and to a smaller extent, three-photon absorption by O₂. Considering the rather long pulse length of the ArF laser (15 ns), further absorption by O₂⁺ will lead to photodissociation of the molecular ion and creation of the detected O⁺ products. Table II lists the lowest dissociation limits of O₂⁺ and their dissociation products along with their molecular states.²⁹

1. One-photon dissociation of O₂⁺

Because the ionic dissociation energy is 6.66 eV, all vibrational states except $v^+=0$ can be photodissociated with one ArF laser photon of 6.4 eV. The low kinetic energy signal in Fig. 3 is assigned to one-photon dissociation of $X^2\Pi_g(v^+=1,2)$ to the O⁺(⁴S)+O(³P) dissociation limit, which correlates with ^{2,4,6}(Σ⁺,Π)_{g,u} states. Since the ionic ground state symmetry is $X^2\Pi_g$, the one-photon allowed states are the $A^2\Pi_u$ and $2^2\Sigma_u^+$, the latter of which is predicted³⁰ to be weakly bound and correlates with the first dissociation limit. There are no known doublet Σ,Π ungerade bound states in the energy region near the first dissociation limit³¹ so the oxygen ion can only photodissociate on the repulsive walls of the $A^2\Pi_u$ and $2^2\Sigma_u^+$ states. This results in a mixture of a parallel and perpendicular transition that should be reflected in the angular distribution of the products. The measured β parameters for the one-photon dissociation of the $X^2\Pi_g(v^+=1)$ and $X^2\Pi_g(v^+=2)$ are 0.43±0.11 and 1.81±0.07, respectively. These β values, which are similar to the ones Parker and Eppink³² measured, indicate a contribution from the $2^2\Sigma_u^+$ state in a direct dissociation process. These values were obtained in the one-color experiment and no difference could be observed in β when the excimer laser was used in small-band or broadband mode.

2. Two-photon absorption by O₂⁺

The set of peaks in the 0.8–1.50 and 2.5–3.5 eV region of Fig. 2 are found to be weaker relative to the one-photon peaks in the 0–0.3 eV region when using broadband light compared to narrowband light, which suggests that they arise from a two-photon excitation process. Two photon excitation of the $X^2\Pi_g(v^+=0,1,2)$ states brings the total energy between 24.9 and 25.6 eV. At these energies all the dissociation limits listed in Table II are energetically accessible. Yet, the closest lying limit, O⁺(²D)+O(¹D) (24.025 eV) is assigned in Fig. 2 as the major one in the kinetic energy spectrum and a small yield in the O⁺(²D)+O(³P) (22.057 eV)

channel can also be seen. A two-photon step starting in the $X^2\Pi_g$ state has the $A^2\Pi_u$ or $2^2\Sigma_u^+$ as intermediate state and would therefore end according to selection rules in a $2^2\Pi_g$, $2^2\Delta_g$, or $2^2\Sigma_g^-$ state. Predissociation or direct dissociation from these molecular states could be responsible for the observed signals, or curve crossing to repulsive states could also take place. Dissociation dynamics in this energy region for oxygen have been studied using one-extreme ultraviolet photon dissociation from the neutral ground state of oxygen $X^3\Sigma_g^-$ by Erman *et al.*³³ Their technique probes one-photon allowed transitions to states that have Franck–Condon overlap with the O₂ ground state. Erman *et al.*³³ measured the energy distributions of O⁺ after XUV photodissociation and found that the maximum KER is less than 2 eV, and the distribution looks similar for the full 24–34 eV energy region. They concluded that the dominant pathway is curve crossing to any dissociative state with good Franck–Condon overlap that correlates with the dissociation limit lying closest to the excitation energy. The present results support this observation.

Beebe, Thulstrup, and Anderson have calculated some states in this region: the $2^2\Sigma_g^-$ (2) at 23.42 eV, the $2^2\Sigma_g^-$ (3) 23.68 eV, and the $2^2\Sigma_g^-$ (4) at 24.89 eV. These states have the proper symmetry $2^2\Sigma_g^-$ for two-step excitation, so the probability of these pathways should be reasonably high. The $2^2\Sigma_g^-$ (4) state lies in the excitation energy region but can not directly dissociate since it correlates with a higher (25.72 eV) limit. This state can couple with other $2^2\Sigma_g^-$ states in order to dissociate. The available $2^2\Sigma_g^-$ states are: the $2^2\Sigma_g^-$ (3) that correlates toward the observed O⁺(²D)+O(¹D) limit, the $2^2\Sigma_g^-$ (2) that correlates towards O⁺(²P)+O(³P) (not seen), and the $2^2\Sigma_g^-$ that has the O⁺(²D)+O(³P) as limit (weakly seen). According to Erman *et al.*³ the closest lying limit is the most probable pathway and therefore the major one seen is the O⁺(²D)+O(¹D) limit.

The results of the anisotropy parameters for the two-photon dissociation channels could be fitted well with a one-photon angular distribution, i.e., the use of only β as a fitting parameter was sufficient. This resulting β values were 1.83±0.39 and 1.74±0.26 for the two-photon dissociation of the $X^2\Pi_g(v^+=0)$ and $X^2\Pi_g(v^+=1)$ state, respectively. Qualitatively, these high values suggest a parallel transition for the first and second steps and it was noted before that the one-photon transition is also nearly parallel. This suggests the intermediate state should have a Π_u character, like the ground state, but then the final state would be a Π_g state and not $2^2\Sigma_g^-$. Several Π_g correlate to the observed dissociation limits including the closest-lying O⁺(²D)+O(¹D) limit. It should be mentioned, however, that other effects such as axis alignment due to photoselection, rotation during dissociation, and coherent versus stepwise two-photon excitation could also play a role in the observed angular distribution anisotropy.

V. CONCLUSION

The angular and kinetic energy distributions of O⁺ atom fragments after O₂ photodissociation with a narrowband tunable ArF were measured and analyzed using the velocity

map imaging technique. Product $O(^3P_2)$ atoms were also detected via (2+1) REMPI with a second laser system. The main $O(^3P_2)$ signals are from two-photon dissociation, one-photon dissociation via the Herzberg continuum, and predissociation following the $B^3\Sigma_u^-(v=4) \leftarrow X^3\Sigma_g^-(v=0)$ transitions. The Herzberg continuum gives an average value of $\beta=0.48$ and the measured β values for the Schumann–Runge bands were in good agreement with previous lifetime measurements of the $B^3\Sigma_u^-(v=4)$ state. $O_2^+ X^2\Pi_g(v^+=0,1,2)$ is formed at the two-photon level at all wavelengths and at several specific wavelengths in the laser tuning range O_2^+ resonances due to (2+1) REMPI via the $n\sigma_g(n-1)d\pi_g^{-1}\Sigma_g^+$ Rydberg states are also observed. The product $O_2^+ X^2\Pi_g$ vibrational states are photodissociated via a one- or two-photon process.

ACKNOWLEDGMENTS

This work was part of the research program of the ‘‘Stichting voor Fundamenteel Onderzoek der Materie (FOM)’’ and is financially supported by the ‘‘Nederlandse Organisatie voor Wetenschappelijk Onderzoek (NWO).’’ The authors thank M. C. van Beek, N. J. Dam, and J. J. ter Meulen for help and use of the tunable excimer laser. The authors also thank C. Sikkens and C. Timmer for technical support.

¹J. F. Noxon and A. E. Johanson, *Planet. Space Sci.* **20**, 2125 (1972).

²A. T. J. B. Eppink and D. H. Parker, *Rev. Sci. Instrum.* **68**, 3477 (1997).

³B. Buijsse, W. J. van der Zande, A. T. J. B. Eppink, D. H. Parker, B. R. Lewis, and S. T. Gibson, *J. Chem. Phys.* **108**, 7229 (1998).

⁴B. R. Lewis, S. T. Gibson, and P. M. Dooley, *J. Chem. Phys.* **100**, 7012 (1994).

⁵E. W. Rothe and P. Andresen, *Appl. Opt.* **36**, 3971 (1997).

⁶S. Yang, W. T. Hill, and S. N. Dixit, *J. Chem. Phys.* **100**, 6434 (1994).

⁷R. N. Zare, *Angular Momentum* (Wiley, New York, 1988).

⁸C. Jonah, *J. Chem. Phys.* **55**, 1915 (1971).

⁹M. Nicolet and R. Kennes, *Planet. Space Sci.* **34**, 1043 (1986).

¹⁰J. P. England, B. R. Lewis, and M. L. Ginter, *J. Chem. Phys.* **105**, 1754 (1996).

¹¹H. Park, P. J. Miller, W. A. Chupka, and S. D. Colson, *J. Chem. Phys.* **89**, 3919 (1988); **89**, 6676 (1988).

¹²A. T. J. B. Eppink, B. L. G. Bakker, and D. H. Parker, *Proc. SPIE* **3271**, 177 (1998).

¹³J. L. Lin, D. W. Hwang, Y. T. Lee, and X. Yang, *J. Chem. Phys.* **109**, 1758 (1998).

¹⁴Y. Huang and R. J. Gordon, *J. Chem. Phys.* **94**, 2640 (1991).

¹⁵A. T. J. B. Eppink, B. Buijsse, M. H. M. Janssen, W. J. van der Zande, and D. H. Parker, *J. Chem. Phys.* **108**, 1305 (1998).

¹⁶D. J. Leahy, D. L. Osborne, D. R. Cyr, and D. M. Neumark, *J. Chem. Phys.* **103**, 2495 (1995).

¹⁷S. T. Gibson, B. R. Lewis, K. G. H. Baldwin, and J. H. Carver, *J. Chem. Phys.* **94**, 1060 (1991).

¹⁸Y. Matsumi and M. Kawasaki, *J. Chem. Phys.* **93**, 2481 (1990).

¹⁹K. Tonokura, N. Shafer, Y. Matsumi, and M. Kawasaki, *J. Chem. Phys.* **95**, 3394 (1991).

²⁰B. Buijsse, W. J. van der Zande, A. T. J. B. Eppink, D. H. Parker, B. R. Lewis, and S. T. Gibson, *J. Chem. Phys.* **108**, 7229 (1998).

²¹G. Groeneboom and A. van der Avoird (unpublished).

²²W. Kong and J. W. Hepburn, *Can. J. Phys.* **72**, 1284 (1994).

²³W. J. van der Zande, W. Koot, J. R. Peterson, and J. Los, *Chem. Phys.* **126**, 169 (1988).

²⁴S. T. Pratt, J. L. Dehmer, and P. M. Dehmer, *J. Chem. Phys.* **93**, 3072 (1990).

²⁵B. L. G. Bakker, G. Meijer, and D. H. Parker (unpublished).

²⁶M. Versluis, G. Meijer, and D. W. Chandler, *Appl. Opt.* **33**, 3289 (1994).

²⁷M. Versluis, Ph.D. dissertation University of Nijmegen, Nijmegen, The Netherlands, 1992; G. Laufer and R. L. McKenzie, AIAA-88-46796-CP, AIAA/NASA/AFWAL Conference on Sensors and Measurements for Aeronautical Applications, Atlanta, 7–9 September 1988 (unpublished).

²⁸B. L. G. Bakker, A. T. J. B. Eppink, and D. H. Parker (unpublished).

²⁹N. H. F. Beebe, E. W. Thulstrup, and A. Andersen, *J. Chem. Phys.* **64**, 2080 (1976).

³⁰C. M. Marian, R. Marian, S. D. Peyerimhoff, B. A. Hess, R. J. Buenker, and G. Seger, *Mol. Phys.* **46**, 779 (1982).

³¹T. Tanaka, H. Yoshii, Y. Morioka, T. Hayaishi, K. Ito, and R. I. Hall, *J. Chem. Phys.* **108**, 6240 (1998).

³²D. H. Parker and A. T. J. B. Eppink, *J. Chem. Phys.* **107**, 2357 (1997).

³³P. Erman, A. Karawajczyk, E. Rachlew-Kallne, M. Stankiewicz, and K. Yoshiki Franzen, *J. Phys. B* **29**, 5785 (1996).